PLASMA EQUIPMENT MODELING FOR PROCESS DESIGN

Mark J. Kushner and Junqing Lu
University of Illinois, Department of Electrical and Computer Engineering
1406 W. Green St., Urbana, IL 61801
mjk@uiuc.edu http://uigelz.ece.uiuc.edu

Abstract

The pace and quality of development of plasma equipment and processing for microelectronics fabrication have improved over the past 5 years due, in part, to the availability of increasingly sophisticated computer models for use as CAD tools. In this paper, the status of plasma equipment modeling will be reviewed and the requirements for further integrating these capabilities into process designed will be discussed.

Introduction

The development of plasma equipment (e.g., reactive-ion-etchers, plasma enchanted chemical vapor deposition systems) has, historically, been performed with little computational support. This situation resulted from a lack of understanding of the important physical processes and, more recently, the lack of databases of basic physical data such as cross sections and transport coefficients. The scientific basis and modeling support for these activities have markedly improved during the past 5 years due the combined efforts of many individuals who have applied diagnostics and first principles modeling to investigation of fundamental phenomena in plasma processing systems. Much of this understanding has been captured in computer aided design tools. Using these CAD tools, the pace and quality of development of plasma equipment and processes have been improved. In this paper, the status of plasma equipment and process modeling will be reviewed, and the requirements for further integrating these capabilities into process designed will be discussed.

Basic Structure of Plasma Equipment Models

One of the fundamental challenges of plasma equipment and process modeling is simultaneously addressing vastly different spatial and time scales. The spatial scales of interest span from reactor dimensions (10s cm to 1 meter) to feature size (sub-micron). The time scales span many to 10's seconds (gas residence times) to sub-ns (plasma oscillation and electromagnetic frequencies). These disparate time and spatial scales are usually addressed by CAD tools which are modular, typically called *hybrid* codes. In a hybrid code, different physical phenomena or time (or spatial scales) are addressed in separate modules, which are iterated to convergence.

One such *hybrid* code developed by our research group, schematically shown in Fig. 1, is the Hybrid Plasma Equipment Model (HPEM).[1-3] In the HPEM, electromagnetics, electron energy transport and heavy particle transport are addressed in different modules. Within each module, different computational methods can be applied to resolve the physical phenomena using techniques appropriate for the operating conditions (e.g., Monte Carlo for low pressure, fluid equations for high pressure). The structure of the HPEM will be described as an overview of the physics typically included in plasma equipment models.

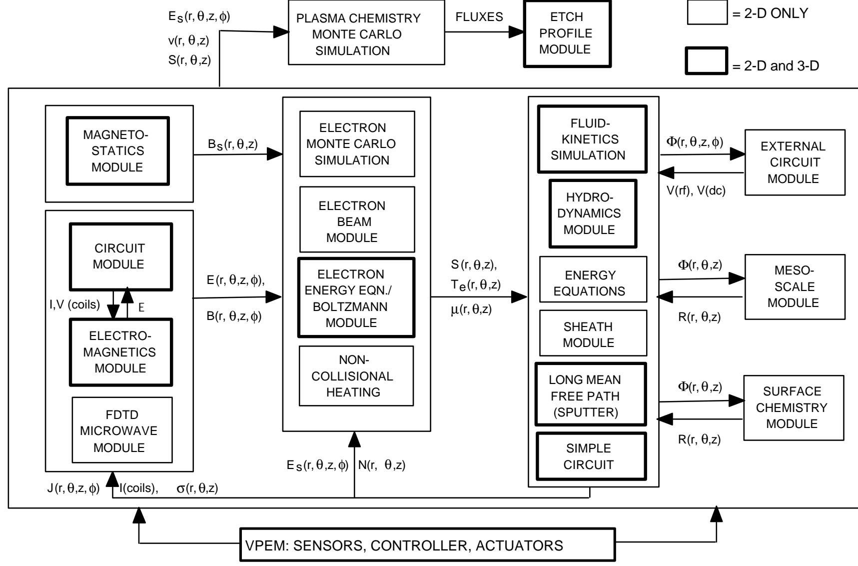

Figure 1 - Schematic of the Hybrid Plasma Equipment Model.

Electromagnetic and magnetostatic fields are obtained in the Electromagnetics Module (EMM). These fields are used in the Electron Energy Transport Module (EETM) to obtain electron impact source functions and transport coefficients. These coefficients are then transferred to the Fluid Kinetics Module (FKM) where the densities, momenta and energy of all heavy particles (ions and neutrals) are obtained. A drift-diffusion formulation is used to obtain electron densities and momenta, which enables a semi-implicit solution of Poisson's equation for the electric potential. A comprehensive circuit model for the reactor and driving electronics is in the FKM, as well as a complete surface kinetics module (SKM) which solves for surface coverages, and reactive sticking coefficients. Densities, fluxes and fields are transferred back to the EMM and EETM, and the process is iterated to convergence.

EMM: Maxwell's equations are solved in the EMM for electromagnetic fields originating from antennas or injected from waveguides. In the former case, the frequency-domain form of Maxwell's equations is solved for the complex vector electric field $\vec{E}\exp(i\omega t)$,

$$\nabla\times\left(\frac{1}{\mu}\nabla\times\vec{E}\right)=-i\omega\bar{\sigma}\cdot\vec{E}-i\omega\vec{j}_c+\omega^2\varepsilon\vec{E}$$

where $\vec{j}_c$ is the external coil current. $\bar{\sigma}$ is the tensor conductivity,

$$\bar{\sigma}=\frac{\dfrac{q^2 n_e}{m_e(i\omega+\nu_m)}}{1+(\alpha B)^2}\begin{pmatrix}1+(\alpha B_r)^2 & \alpha B_z+\alpha^2 B_r B_\theta & -\alpha B_\theta+\alpha^2 B_r B_z\\ -\alpha B_z+\alpha^2 B_r B_\theta & 1+(\alpha B_\theta)^2 & \alpha B_r+\alpha^2 B_\theta B_z\\ \alpha B_\theta+\alpha^2 B_r B_z & -\alpha B_r+\alpha^2 B_\theta B_z & 1+(\alpha B_z)^2\end{pmatrix}$$

where $\alpha=q/((i\omega+\nu_m)m_e)$ and ν_m is the momentum transfer collision frequency. The static magnetic field components are obtained by solving for the vector potential, $\nabla\times\left(\mu^{-1}\nabla\times\vec{A}\right)=\vec{J}$, $\vec{B}=\nabla\times\vec{A}$. For Helmholtz coils $\vec{J}$ is the current density in the coils. For permanent magnets, the magnetic material is resolved as a superposition of small current loops. These equations are implicitly solved using the method of Successive-Over-Relaxation (SOR), which is typically stable for solutions in the near field. In the case of injected waves or conditions which are in the intermediate or far field, such as in an Electron Cyclotron Resonance reactor, conjugate gradient methods are used or Maxwell's equations are directly solved using the Finite-Difference-Time-Domain method.[4]

In the EETM, electron impact source functions and transport coefficients are obtained. The EETM consists of two options. The Electron Monte Carlo Simulation (EMCS) can be used to obtain electron energy distributions as a function of position. This is a fully kinetic treatment which resolves the gyro-motion of electrons in magnetic fields using a semi-implicit technique. Non-collisional heating is kinetically resolved by producing electron currents which are used to correct the assumption of collisional power deposition in the EMM.[5] The second option is to solve the electron energy equation for the electron temperature $kT_e = 2/3\bar{\varepsilon}$. Transport coefficients as a function of average energy $\bar{\varepsilon}$ are obtained from solutions of Boltzmann's equation. The conservation equation we solve is:

$$\frac{\partial\left(\frac{3}{2}n_e kT_e\right)}{\partial t} = \nabla\cdot\bar{\kappa}\nabla T_e - P_e - \nabla\cdot\left(\frac{5}{2}kT_e\vec{\phi}_e\right) - S_e$$

where n_e is the electron density, $\bar{\kappa}$ is the tensor electron thermal conductivity, P_e is power input from Joule heating or beams, S_e is for collisional losses and $\vec{\phi}_e$ is the electron flux from the FKM. This equation is implicitly solved in the steady state using SOR. Secondary electron emission from surfaces is still resolved using the MCS.

In the FKM, there are options to solve heavy particle transport (ions and neutrals) using 1st, 2nd and 3rd moments of Boltzmann's equations for continuity, momenta and energy:

$$\frac{\partial N_i}{\partial t} = -\nabla\cdot\vec{\phi}_i + S_i$$

$$\frac{\partial\left(m_i\vec{\phi}_i\right)}{\partial t} = \nabla P - \nabla\cdot\left(\vec{v}_i\vec{\phi}_i\right) + q_i m_i N_i\left(\vec{E} + \vec{v}_i\times\vec{B}\right)$$

$$-\nabla\cdot\bar{\tau} + \sum_j \frac{m_i m_j}{m_i + m_j} N_i N_j \nu_{ij}\left(\vec{v}_j - \vec{v}_i\right)$$

$$\frac{\partial N_i c_v T_i}{\partial t} = \nabla\cdot\kappa_i\nabla T_i - P_i\nabla\cdot\vec{v}_i - \nabla\cdot(\vec{\phi}_i\varepsilon_i)$$

$$+\frac{N_i q_i^2}{m_i\nu_i}E_s^2 + \frac{N_i q_i^2\nu_i}{m_i(\nu_i^2 + \omega^2)}E^2$$

$$+\sum_j 3\frac{m_{ij}}{m_i + m_j}N_i N_j R_{ij} k(T_j - T_i)$$

where, for neutral species, τ is the viscosity tensor. Each species is treated separately in terms of momenta and energy, and so exchange terms between species are included. Slip boundary and temperature jump conditions are employed as required. Electron densities are obtained using a drift-diffusion formulation with tensor resolved transport coefficients:

$$\frac{\partial n_e}{\partial t} = -\nabla\cdot\phi_e + S_e$$

$$\vec{\phi}_e = \bar{T}\cdot\left(-n_e\mu_o\vec{E} - D_o\nabla n_e\right)$$

$$\bar{T} = \frac{1}{\left(1+\mu_o B^2\right)}\begin{pmatrix} 1+\mu_o^2 B_r^2 & \mu_o B_z + \mu_o^2 B_r B_\theta & -\mu_o B_\theta + \mu_o^2 B_r B_z \\ -\mu_o B_z + \mu_o^2 B_r B_\theta & 1+\mu_o^2 B_\theta^2 & \mu_o B_r + \mu_o^2 B_\theta B_z \\ \mu_o B_\theta + \mu_o^2 B_r B_z & -\mu_o B_r + \mu_o^2 B_\theta B_z & 1+\mu_o^2 B_z^2 \end{pmatrix}$$

The electric potential Φ is obtained by solving a semi-implicit form of Poisson's equation which predicts the charge density ρ at future times. With the ion momentum option, we solve:

$$-\nabla\cdot\varepsilon\nabla\Phi\left(t+\Delta t\right) = \rho\left(t\right) + \frac{d\rho\left(t'\right)}{dt}\Delta t$$

$$\frac{d\rho\left(t'\right)}{dt} = -q\left(-\bar{T}\cdot\left(-n_e(t)\mu_o\left(-\nabla\Phi\left(t+\Delta t\right)\right) - D_o\nabla n_e(t)\right)\right) + \sum_j -q_j\nabla\cdot\vec{\phi}_j(t)$$

Alternately, the electric potential can be obtained assuming ambipolar transport by solving an analogous Poisson-like equation. When the mesh is unable to resolve the sheath, a semi-analytic sheath model is used to "insert" a jump boundary condition in electric potential at the interface between the plasma and surfaces.

Although hybrid codes have been quite successful in resolving *quasi-steady state* phenomena (e.g., steady state but time resolved radio frequency excitation), their serial iterative nature makes it difficult to

resolve true transients occurring over long periods of time (e.g., 10's seconds startup or shutdown transient). Advanced computational techniques in which modules are performed in parallel are addressing these needs.

In simulating sputter deposition sources the long mean free path of sputtered atoms must be accounted for. This is accomplished using a Monte Carlo simulation for the sputtered atoms slowing in the gas. [3] This produces a Green's function, $G(\vec{r},\vec{r}')$, for the rate of thermalization of sputtered atoms at $\vec{r}$ in the volume for a given ion current density j at $\vec{r}'$ on the target. The total rate is then $R(\vec{r}) = \oint G(\vec{r},\vec{r}')j(\vec{r}')dA'$. Since the operating conditions are in the linear cascade regime of collisional sputtering the spectrum of sputtered atoms of energy E is obtained from [6]

$$F(E) = 2\left(1 + \frac{E_b}{\Lambda E_i}\right)^2 \frac{E_b E}{(E + E_b)^3}$$

for energies $E < \Lambda E_i$ where E_b is the binding energy of the target material, E_i is the incoming ion energy, and $\Lambda = 4m_i m_T/(m_i + m_T)$, for m_i and m_T being the mass of the ion and target atoms. We assume that the difference in the sputtered atom kinetic energy before and after a collision is converted to random thermal energy of the background gas which then produces "sputter heating" and rarefaction.[7,8]

The final quantity of interest is, in large part, the properties of surfaces (e.g., deposited films or evolved feature profiles) which result from plasma generated fluxes of reactants interacting with those surfaces. Plasma equipment models therefore contain detailed surface chemistry models and profile simulators or are coupled to profile simulators as post processors. Monte Carlo profile simulators have become popular in this regard due to their ability to address user defined reaction chemistries which allow modeling of polymer passivation and etch stops as encountered in fluorocarbon etching of SiO_2.

Modeling of Ionized Metal Physical Vapor Deposition

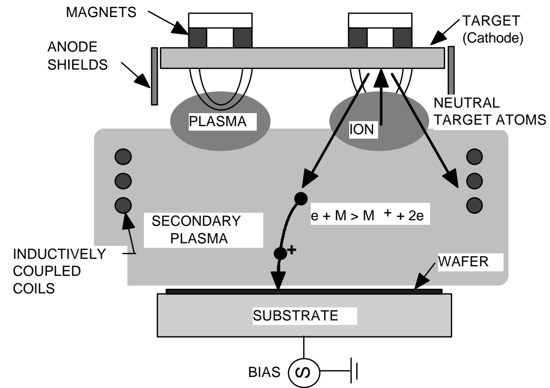

Figure 2 - Schematic of an IMPVD reactor using a planar magnetron and an ICP as an auxiliary ionization source.

As a demonstration of current capabilities in plasma equipment and process modeling, results from the HPEM will be shown for Ionized Metal Physical Vapor Deposition (IMPVD).[9,10] IMPVD is used to deposit conformal metal seed layers or fill trenches with metal for interconnect while avoiding formation of voids. This is accomplished by having a significant fraction of the metal atoms flux incident onto the substrate be ionized, thereby providing an anisotropic flux. Some amount of sputtering of overhangs also occurs. The reactor typically used for IMPVD consists of a planar magnetron sputter source and a secondary plasmas sustained by inductively coupling, as shown in Fig. 2.[11] The operating pressure is typically 10s mTorr, as opposed to a few mTorr in a PVD tool, which is sufficiently high that sputtered atoms are stopped in the gas before reaching the substrate. The thermal metal atoms are then ionized by the secondary plasma.

Results from the HPEM for IMPVD of Cu using an argon secondary plasma are shown in Fig. 3. The reactor uses a ring magnetron and a copper target to sputter copper atoms into the plasma.[11] The magnetron power is 300 W. The inductively coupled plasma (ICP) is generated by coils immersed in the plasma and produces power deposition of 1 kW. The Ar buffer gas pressure is 40 mTorr. The substrate is biased at -25 V.

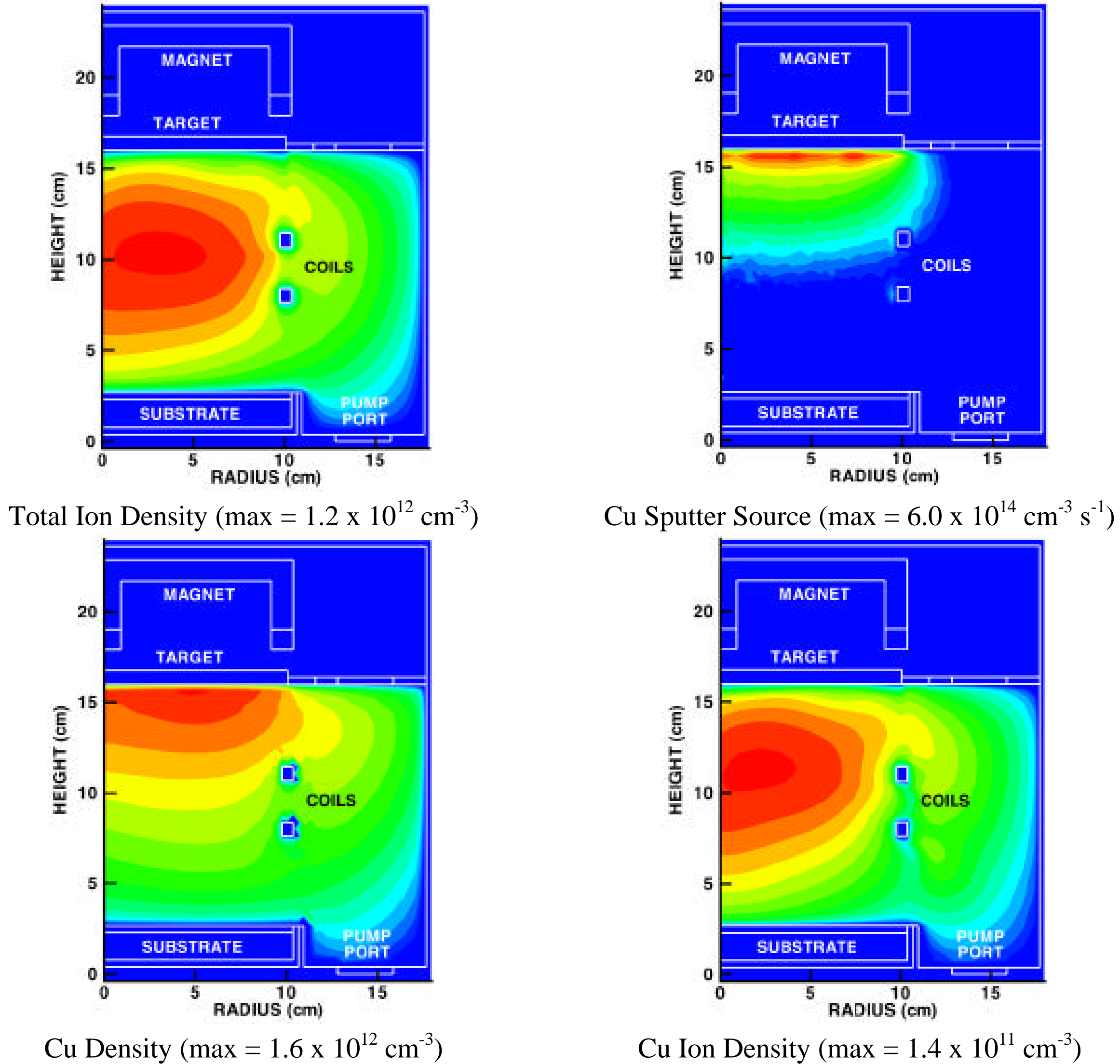

Total Ion Density (max = 1.2×10^{12} cm^{-3})

Cu Sputter Source (max = 6.0×10^{14} cm^{-3} s^{-1})

Cu Density (max = 1.6×10^{12} cm^{-3})

Cu Ion Density (max = 1.4×10^{11} cm^{-3})

Figure 3 - Plasma properties for an IMPVD reactor for deposition of Cu. (top left) Total ion density, (top right) Sputter source for Cu atoms, (bottom left) Total density of neutral Cu, and (bottom right) Cu ion density. Each figure is a 2-decade log plot with the maximum value listed at the bottom of the figure.

The total ion density peaks at 1.2×10^{12} cm^{-3}. The ion flux to the target produces a sputter source of Cu atoms which are slowed in the gas within about 5 cm. This source produces a neutral Cu density of 1.6×10^{12}, which diffuses to the substrate. During the Cu transport to the substrate, electron impact ionization occurs, producing a Cu ion density of 1.4×10^{11} cm^{-3}, or about 10% of the total ion density. Due to the high mobility of ions

compared to the neutrals, these densities produce a copper flux to the substrate which is about 80% ions.

The filling of trenches in SiO_2 with copper by IMPVD, as obtained with the Monte Carlo Feature Profile Model, is shown in Fig. 4. Profiles are shown for pressures of 5, 20 and 40 mTorr. Over this range of pressure, the fill changes from having a large central void to being solid. The cause of the improved fill factor is an increase in the fraction of the incident metal flux which is ionized with increasing pressure. This fraction increases from 25% at 5 mTorr to 80% at 40 mTorr. The larger ion fraction produces a more anisotropic flux of metal atoms into the feature as a result of ion acceleration in the sheath above the wafer. There is also additional self sputtering and redeposition which reduces the overhang at the top of the trench.

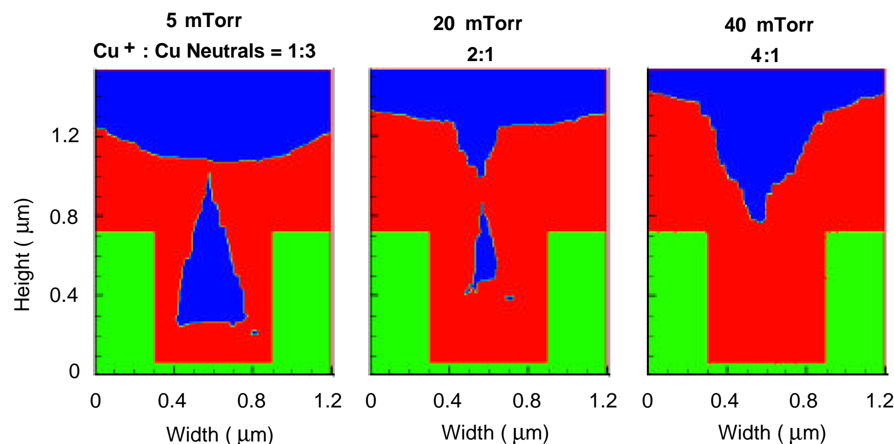

Figure 4 - Simulation of trench filling with Cu using IMPVD at pressures of 5, 20 and 40 mTorr. The filling of the void results from an increase in the fraction of ionized copper atoms in the incident fluxes.

Concluding Remarks

Plasma equipment and process modeling has significantly advanced in the past 5 years due to improvements in our understanding of the important physics and due to improvements in computational capabilities. Databases of fundamental data, such as cross sections and sticking probabilities, will need to improve in order for the impact of modeling on process design to continue to increase.

Acknowledgments

This work was supported by the National Science Foundation (CTS 99-74962), Semiconductor Research Corp. and DARPA/AFOSR.

References

1. X. Xu, S. Rauf and M. J. Kushner, J. Vac. Sci. Techol. A, **18**, 213 (2000).
2. D. Zhang and M. J. Kushner, J. Appl. Phys., **87**, 1060 (2000).
3. J. Lu and M. J. Kushner, J. Appl. Phys., **87**, 7198 (2000).
4. R. L. Kinder and M. J. Kushner, J. Vac. Sci. Technol. A **17**, 2421 (1999).
5. S. Rauf and M. J. Kushner, J. Appl. Phys. **81**, 5966 (1997).
6. V. V. Serikov and and N. Nanbu, J. Vac. Sci. Techol. A, **14**, 3108 (1996).
7. S. M. Rossnagel, J. Vac. Sci. Techol. B, 1**6**, 3008 (1998).
8. M. Dickson, F. Qian, and J. Hopwood, J. Vac. Sci. Techol. A, **15**, 2161 (1997).
9. S. M. Rossnagel, Semicond. Int. 21, 99 (1996).
10. S. M. Rossnagel and J. Hopwood, J. Vac. Sci. Techol. B, **16**, 499 (1998).
11. P. F. Cheng, S. M. Rossnagel, and D. N. Ruzic, J. Vac. Sci. Techol. B, **13**, 203 (1995).